


 Cite this: *Lab Chip*, 2024, 24, 707

Single-cell fluid-based force spectroscopy reveals near lipid size nano-topography effects on neural cell adhesion†

 Zeina Habli, ^a Rima Lahoud,^a Ahmad Zantout,^a Wassim Abou-Kheir^b and Massoud L. Khraiche ^{*a}

Nano-roughness has shown great potential in enhancing high-fidelity electrogenic cell interfaces, owing to its characteristic topography comparable to proteins and lipids, which influences a wide range of cellular mechanical responses. Gaining a comprehensive understanding of how cells respond to nano-roughness at the single-cell level is not only imperative for implanted devices but also essential for tissue regeneration and interaction with complex biomaterial surfaces. In this study, we quantify cell adhesion and biomechanics of single cells to nano-roughened surfaces by measuring neural cell adhesion and biomechanics *via* fluidic-based single-cell force spectroscopy (SCFS). For this, we introduce nanoscale topographical features on polyimide (PI) surfaces achieving roughness up to 25 nm without chemical modifications. Initial adhesion experiments show cell-specific response to nano-roughness for neuroblastoma cells (SH-SY5Y) compared to human astrocytes (NHA) around 15 and 20 nm surface roughness. In addition, our SCFS measurements revealed a remarkable 2.5-fold increase in adhesion forces (150–164 nN) for SH-SY5Y cells cultured on roughened PI (rPI) surfaces compared to smooth surfaces (60–107 nN). Our data also shows that cells can distinguish changes in nano-roughness as small 2 nm (close to the diameter of a single lipid) and show roughness dependence adhesion while favoring 15 nm. Notably, this enhanced adhesion is accompanied by increased cell elongation upon cell detachment without any significant differences in cell area spreading. The study provides valuable insights into the interplay between nano-topography and cellular responses and offers practical implications for designing biomaterial surfaces with enhanced cellular interactions.

 Received 14th November 2023,
 Accepted 27th December 2023

DOI: 10.1039/d3lc00984j

rsc.li/loc

1. Introduction

The neuron-artificial substrate interaction is a determinant of implant life and signal quality.^{1–3} Nano-topography provides a unique interface for neurons, when at the scale of its proteins and lipids, and has shown great promise in advancing high-fidelity electrogenic cell interfaces *via* improving cell-substrate adhesion. The latter can enhance signal transmission, as proximity to the surface facilitates efficient communication between neurons and the substrate electrodes potentially leading to improved signal transfer and high signal-to-noise ratio. Also, neurons that are tightly adhered to a surface are less likely to detach or move around, providing

greater stability to neural networks. This stability is particularly beneficial in long-term studies or implantable devices where consistent neural connectivity and signal recording are desired.

Polyimide (PI) is an attractive flexible aromatic polymer with robust chemical and thermal stability and has been extensively used in fabricating mechanically compliant neural prosthetics in both research and clinical applications.^{4,5} The biocompatibility of PI and other polymers is a complex endeavour and there is evidence that it is directly influenced by its chemical structure and/or surface topography.⁶ Yet, biocompatibility alone does not guarantee the implantation's success; the latter is governed by proper implant integration with the brain tissue *via* cell-surface interaction, which can be ameliorated *via* surface modifications. However, PI still lacks cell-interactive properties and thus requires surface modifications to improve cell proliferation and adhesion responses.⁷ Since PI sheets are soft, their topography can be tailored by laser ablation, dry oxygen plasma etching, and reactive ion etching; these are known to (1) enhance PI surface wettability and (2) induce surface roughness.^{8–10} In

^a *Neural Engineering and Nanobiosensors Group, Biomedical Engineering Program, Maroun Semaan Faculty of Engineering and Architecture, American University of Beirut, Beirut 1107 2020, Lebanon. E-mail: mkhraiche@aub.edu.lb*

^b *Department of Anatomy, Cell Biology and Physiological Sciences, Faculty of Medicine, American University of Beirut, Beirut 1107 2020, Lebanon*

† Electronic supplementary information (ESI) available. See DOI: <https://doi.org/10.1039/d3lc00984j>

fact, PI with chemically induced nano-ordered surface roughness has been shown to induce fibrinogen adsorption, prompt platelet adhesion, and improve fibroblast proliferation and adhesion.^{10,11} Nonetheless, very few studies have investigated the biophysical response and quantitative relationship between the surface roughness of polymers and neural cell adherence for neural implant applications. One study by Jackson *et al.* showed that the roughness of Aluminium nitride (AlN)/PI films (~8 nm) significantly improves the proliferation and adhesion of primary neurons.¹² In another study, Kawakami *et al.* reported that PC-12 neural cells proliferated and differentiated better and had increased neurite growth when cultured on roughened ion-radiated PI films.¹³

Neural cell attachment and adherence is an orchestrated process that involves the association of focal adhesion complexes with the subsequent substratum material. It is well known that neural cells can sense topographical features as external stimuli and interact with changes in the mechanical cues by adjusting their mechanical state when placed in proximity to foreign substrates (*i.e.*, altering their shape, modulating their cellular elasticity, and realigning their cytoskeletal architecture).^{14–17} Within this context, nano-roughness may play a role in modulating neural cell adhesion and process. Several approaches have been exploited for the quantitative analysis of cell adhesion and mechanical properties. The gold standard is the high-precision sensitive Single-Cell Force Spectroscopy (SCFS) technique which was initially developed on atomic force microscopy (AFM). However, many limitations have been associated with AFM-based SCFS, mainly the need to use chemical bonds which may alter cellular processes and difficulties in detaching cells with mature intercellular junctions (the process is time-consuming with low output).^{18–20} FluidFM technology (fluidic force microscopy) is a novel versatile tool developed to overcome AFM limitations and to study cell adhesion and mechanics under physiological conditions with high throughput. The robotized FluidFM facilitates SCFS by combining AFM technology with micro-channelled cantilevers and fluid pressure controls to completely detach the cells under study.^{21,22} FluidFM-based SCFS has been used to assess adhesion forces of mammalian cell lines to underlying substrates enabling label-free, rapid, and reliable adhesion detachment recordings while providing a high signal-to-noise ratio without altering cell physiological properties.^{23–30}

In this work, we measure the impact of nanoscale surface roughness on single-cell neural adhesion and mechanical coupling to underlying substrates. We optimized plasma treatment to produce a reproducible process capable of tailoring precise polyimide surface roughness with no chemical modification. To investigate cell type and cell-substrate specific behavior, we chose SH-SY5Y neuroblastoma cells and Normal Human Astrocytes (NHA) as *in vitro* models for our work. Both cell lines have shown high sensitivity to

variations in nanometer-ordered surface roughness.^{31,32} Tissue culture plastic (TCP) and glass coverslips (GC) were used as control surfaces for both cell lines. First, we evaluated the initial adhesion responses of both neurons (SH-SY5Y cells) and glia (NHA) cells. Then, we quantified in depth the adhesion force and mechanical properties of the nanoscale-sensitive SH-SY5Y cells using FluidFM technology by completely detaching cells from their substrates, measuring their adhesion forces, and probing their biomechanical properties. We compared the biomechanical cues of neurons cultured on the roughened PI surfaces to that of neurons cultured on smooth PI and TCP substrates. Such quantification of neural cell-substrate adhesion is crucial to expand our knowledge and understanding of the neural biological responses to surface nano-topography and, potentially, will give us insights into enhancing neural interface designs.

2. Materials and methods

2.1. Polyimide sample preparation

Dupont™ Kapton® polyimide (PI) adhesive sheets (50 μm thickness) were cut and tightly pressed on ethanol-cleaned glass squared coverslips (GC) (22 × 22 mm) to prevent bubble formation and surface scratches. The PI surface was then rinsed with 70% ethanol, dried with N₂ gas, and wiped with KimWipes (Kimtech Science) to remove any surface artifacts.

2.2. Polyimide plasma etching

For dry etching, an oxygen plasma etcher (PE-25 Series Plasma System, USA) was used to modify and roughen the PI surfaces. Oxygen gas was fed into the chamber at a flow rate between 15–55 cc min⁻¹, and the vacuum pressure was pre-set between 80–200 mTorr. As the chamber stabilizes at the pre-set desirable values after the oxygen gas flow, Radio Frequency (RF) power for plasma etching was applied and maintained between 100–150 W to promote a high etch rate. The PI surface etching was carried out between 30 sec and 1 hour, after which the PI samples were submerged in distilled water at 37 °C and dried on a hotplate for 30 min to induce greater roughness values.

2.3. Surface roughness measurements and topography characterization

Pristine, plasma-treated PI and TCP samples were cleaned using ethanol with a final rinse of distilled water, and then dried with N₂ gas to remove any surface artifacts. The roughness profile readings were obtained using a 2D high-resolution DektakXT® stylus profilometer (Burker, USA) at 0.167 μm pt⁻¹ scan speed to evaluate a 1 mm length sample. The filtered roughness of each measurement was obtained by a Gaussian regression with a long cutoff at 0.08 mm. At least ten measurements were taken at different locations on each PI sample, and at least three different samples per condition were assessed. The arithmetic average roughness (Ra) was

recorded using the Vision 64 software. A Digital Holographic Microscope (DHM®, Lyncée Tec, Switzerland) with holographic interferometry technology was used to characterize the surface topography of plasma-treated PI sheets in an optical non-contact mode.

2.4. Contact angle measurement

A standard goniometer OCA 15EC (Dataphysics, Germany) was used to assess each PI-treated sample surface wettability (via contact angle measurement) with the sessile drop method. Wettability was measured by dripping 5 μL distilled water droplets to each surface at a speed of 1 $\mu\text{L sec}^{-1}$ and measuring the angle formed between the droplet and the surface of the sample. Measurements were taken 10 sec after the water droplet was introduced into the PI surface to maintain consistency. SCA20 software (Dataphysics, Germany) was used to measure the contact angles. At least three different PI samples were analyzed per plasma treatment condition with five drops each. The contact angles were measured directly after plasma treatment and five days post-treatment (stored in dry conditions) to evaluate the wettability of the treated substrates over time.

2.5. Characterization using spectrometric analysis

The absorption spectra of pristine and plasma-treated PI substrates were investigated at room temperature using Transmission Fourier Infrared Spectroscopy (FT-IR) on a Burker Fourier transform infrared spectrophotometer equipped with a class 1 laser. The measurements were carried out in the range of 1000 to 4000 cm^{-1} in transmission mode with a resolution of 4 cm^{-1} and 32 scans per sample. The obtained spectra were baseline-corrected and normalized to account for variations in the samples.

2.6. Cell culture

Undifferentiated human SH-SY5Y neuroblastoma cells, between passages 20 and 35 were maintained on tissue culture plastic plates (TCP) (Falcon®, USA) in Dulbecco's Modified Eagle Medium (DMEM) F12 Ham supplemented with 10% Fetal Bovine Serum (FBS), 1% sodium pyruvate, 1% non-essential amino acid, 1% penicillin-streptomycin (P/S) and 0.2% plasmocin prophylactic at 37 °C and 5% CO₂ in a humidified incubator. Unless otherwise stated, the cells were seeded at a density of 1.5×10^5 cells per mL. Normal Human Astrocytes (NHA) were maintained in Astrocyte Basal Media (ABM) supplemented with 10% FBS and 1% P/S at 37 °C and 5% CO₂ in a humidified incubator. For the adhesion and viability experiments, the NHA cells were seeded on substrates (TCP or PI) coated with Poly-L-Lysine (PLL).

2.7. Initial cell adhesion assessment

SH-SY5Y and HNA cells were seeded at a density of 0.4×10^6 and 2.3×10^4 cells per well, respectively, in 6-well plates (353046, Falcon®, USA). The well plate contained either a

plasma-treated PI sample, GC, or no GC where cells grow directly on the regular TCP as a control. The PI samples and GC substrates were attached to the TCP wells using a double-sided tape to prevent their movement. For initial adhesion, the cells were seeded on the corresponding substrates and incubated for 2 h, after which the media was changed to remove unbound, loosely bound, and floating cells. The substrates were moved to new wells and adhered cells were trypsinized and counted. Initial cell adhesion was expressed as the percentage of cells adhered with respect to the initial number of cells seeded.

2.8. Immunofluorescence staining

SH-SY5Y cells cultured on glass coverslips (22 mm \times 22 mm) for 72 hours were fixed with 4% paraformaldehyde (PFA), permeabilized with 0.1% Triton-X, and blocked with 3% normal goat serum (NGS) for 1 h at room temperature. Primary antibodies used were rabbit polyclonal antibodies against Focal Adhesion Kinase-FAK (ab131435, 1:200, abcam) and rabbit polyclonal antibodies against phospho-paxillin (Tyr118 2541, 1:100, Cell Signaling). Secondary goat anti-rabbit antibodies conjugated with Alexa Fluor 594 (Thermo Fisher, Invitrogen) and phalloidin conjugated with Alexa Fluor 488 (A12379, Thermo Fisher, Invitrogen) were used at the manufacturer's proposed dilutions. The nuclei were counterstained with 4,6-diamidino-2-phenylindole (DAPI) and the glass coverslips were then mounted on microscopic glass slides. The cells were then examined and imaged with a laser-scanning confocal microscope (Zeiss, LSM710).

2.9. Prominent cell adhesion assessment by fluidic force microscopy: single cell adhesion spectroscopy and calibrations of probes

All the SCFS measurements were carried out using the FluidFM instrument (Cytosurge AG., Zurich, Switzerland) set on a vibration-free table (note: the robotized FluidFM was called BOT, but currently, the company titled it OMNIUM) with a FluidFM micropipette cantilever (Cytosurge AG., Zurich, Switzerland) having an aperture of 8 μm and a nominal spring constant of 2 N m^{-1} . Before every experiment, the cantilever spring constant (k [N m^{-1}]) was calibrated using the Sader method by a build-in function in the OMNIUM system³³ and the inverse optical lever sensitivity ($InvOLS$ [$\mu\text{m V}^{-1}$]) was determined based on the position of the laser reflection optics of the instrument. The bending of the cantilever was measured by optical beam deflection (OBD), and the position of the beam on a photodetector (deflection signal) was measured in volts (V). The force of adhesion (F [N]) is directly proportional to the deflection of the cantilever provided by the photodetector in the form of an electric signal and can be derived from the following equation: $F = k \times InvOLS \times V$. The maximum deflection of the cantilever during the retraction corresponds to the maximum detachment force (maximum peak in the force-distance curve), which is used to represent the adhesion force (F_{adh} in

nN). Using the obtained force–distance (F – D) curves, the detachment work (W_{adh} in pJ) can be calculated from the area demarcated by the force curve, and it represents the binding energy of the cell with the surface. In addition, the maximum detachment distance (D_{max} in μm) required to pull the cell from the surface can be obtained; it's measured from the initial point of cell-cantilever contact when the cantilever starts to deflect and extends to the point the cantilever regains its original shape.

SH-SY5Y and NHA cells were seeded in a 6-well plate at a density of 2×10^5 cells per mL either on a plasma-treated PI sample with varying roughness ($R_a \cong 3$ nm, 15 nm, or 25 nm) or directly on the regular TCP as a positive control with a working volume of 2 mL. After 24 h, the 6-well plates were loaded into the OMNIUM system encompassed by a humidified incubator kept at 37 °C during the whole experiment. Prior to the force measurements, the hollow micropipette cantilever was filled with 1 μL buffer of Milli-Q water: glycerol (1 : 1 ratio). For force adhesion measurements, the cantilever is set to approach a chosen cell at its central region as the landing position while maintaining +20 mbar pressure to prevent unwanted media components or cell debris from entering the cantilever's aperture. The approach speed of the cantilever was set at 1 $\mu\text{m s}^{-1}$ until the deflection of the photodetector voltage reaches 25 mV, at this stage, the cantilever contacts the cell and is kept static for 5 sec while applying a negative pressure of –300 mbar to ensure the sealing of the cell to the cantilever. As the cantilever retracts while applying the negative pressure, it bends downwards. Once the force required to bend the cantilever exceeds the maximum cell adhesion force, rupture events happen causing the cell to fully detach from the surface and the cantilever to return to its original shape. The retraction distance of the cantilever after the cell detachment event was maintained at 50 μm for all experiments at a speed of 1 $\mu\text{m s}^{-1}$. The same parameters were fixed for the measurements taken of all the selected individual SH-SY5Y and in control TCP and rPI. The selection criteria were mainly that these cells should be free of any cellular contact (single cells) to measure their cell–substrate forces. Between every adhesion measurement, the cantilever attached to the plastic holder, known together as the probe, was cleaned for a few minutes with 5% hypochlorite, then rinsed three times with Milli-Q water followed by cell culture media. The cleaning process was done frequently to prevent the accumulation of cell debris and extracellular matrix on the cantilever tip. Including cleaning, a maximum of 6 to 8 cells can be measured per hour, and between 30 and 50 cells per condition were analyzed from three independent replicates.

2.10. Data evaluation and statistical analysis

Analysis of the obtained SCFS data was carried out using AtomicJ and a custom MATLAB code to evaluate the characteristic F – D curves and calculate the F_{adh} , W_{adh} , and D_{max} . Cell area (A_{cell}) of individual cells was calculated in

ImageJ by manually drawing the outline shape of the cell after calibrating the scalebar. The area was defined based on microscopic images taken directly before cell detachment. Lognormal and normal distribution curve fitting, data plots, and significance tests were carried out in GraphPad Prism 8.0.1 and OriginPro 9.5. For the raw data, which was not normally distributed, outliers were removed using the ROUT method with a significance level of 0.05 and accordingly discarded. Since the obtained data is rather lognormally distributed in most parameters, a non-parametric two-sample Mann Whitney (unpaired, unequal variances) test was then applied ($\alpha = 0.05$) to the lognormally distributed data sets. Significance levels were assigned by * for $p < 0.05$, ** for $p < 0.01$ and *** for $p < 0.001$. Results of normality and lognormality tests, histogram of lognormal distributions, linear regressions, spearman correlations, and other relevant data are shown in supplementary data.

3. Results and discussion

3.1. Surface properties of PI substrates: roughening effects

3.1.1. Surface roughness. Results in Fig. 1 show plasma-treated PI samples at different vacuum pressures, bias power values, oxygen flow rates, and duration periods. The treatment process was optimized to control PI surface roughness with no chemical modification. First, the effect of oxygen flow rate and plasma treatment time on the variation of PI surface roughness was investigated. As seen in Fig. 1a, for fixed RF bias power at 100 W and pressure at 200 mTorr, the surface roughness of plasma-treated PI sheets increased with increasing the plasma treatment time. On the other hand, oxygen flow had little impact from 15 cc min^{-1} to 50 cc min^{-1} . Before etching, the roughness of untreated PI sheets (pristine PI) was measured to be around 2.5 nm, after etching at 15 cc min^{-1} oxygen flow rate, the roughness increased up to $\cong 9$ nm at 40 min of plasma exposure. However, at 25 cc min^{-1} and 50 cc min^{-1} oxygen flow rates, the increase in surface roughness was limited to only 6.5 nm and 4.3 nm, respectively. This is expected as increasing the amount of oxygen usually impedes the roughening effects of plasma.³⁴

Second, the influence of pressure and plasma exposure duration on surface roughness was investigated. The 15 cc min^{-1} oxygen flow rate was chosen for this set of experiments because it resulted in greater roughness values compared to higher flow rates. To enhance the etching intensity, the bias power was ramped up to 150 W but kept within the low bias power density range. This technique was adapted to prevent over-etching of the PI surfaces, which can occur under high-energy ion bombardment. The latter causes chain scissions on the PI surface and weakens its boundary layers by removing its outer chemically active layer.^{35,36} For a given pressure, extending the time of plasma exposure increased the roughness approximately in a linear manner, but the roughness trend showed reduced values at higher vacuum pressures. For example, PI substrates treated with plasma at vacuum pressures of 80, 100, or 200 mTorr for 10 min

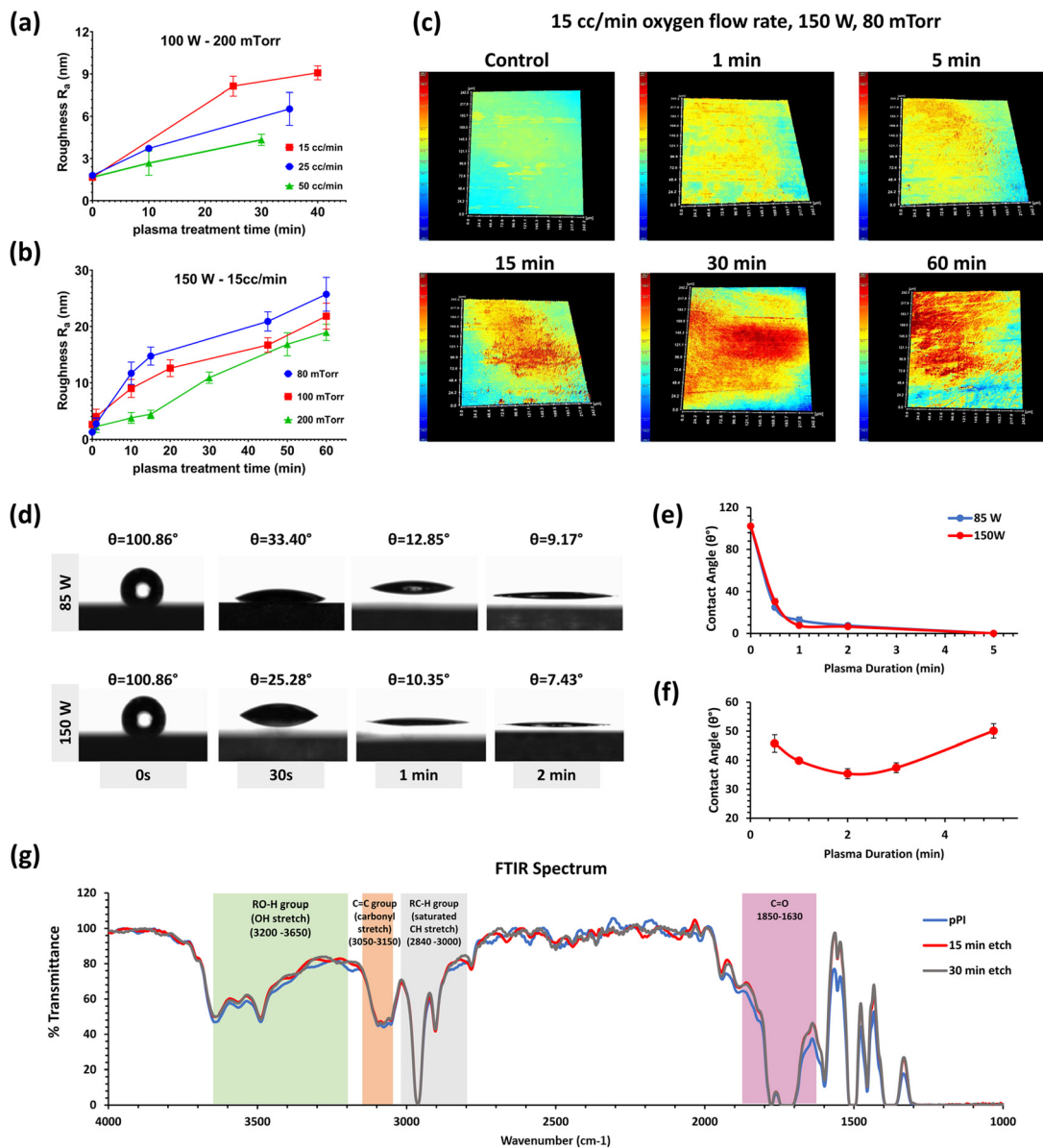


Fig. 1 Surface roughness, wettability, and chemical modifications of plasma-treated polyimide at different times, power ranges, and oxygen flows. PI substrates were cleaned and etched using oxygen plasma at different vacuum pressures, powers, and time points. (a) Surface roughness of oxygen-treated PI surfaces at 100 W, 200 mTorr, and different oxygen flows. (b) Surface roughness of oxygen-treated PI surfaces at 150 W, 15 cc min⁻¹ oxygen flow, and different power ranges. (c) Holographic images of oxygen-treated PI surfaces at 200 mTorr, 15 cc min⁻¹, and 150 W. (d) Sessile water drop profile on oxygen-treated PI surfaces with the corresponding average contact angle. (e) Average contact angle of oxygen-treated PI surfaces at 85 W and 150 W with different time points. (f) Average contact angle measurements on oxygen-treated PI surfaces (up to 5 min at 150 W) 5 days post-treatment. (g) FTIR spectra of pristine polyimide (pPI) and oxygen plasma-etched polyimide samples show no chemical change due to etching.

exhibited surface roughness values of 11.69 nm, 9 nm, and 3.37 nm, respectively. Extending the plasma treatment to 1 h led to a substantial rise in average surface roughness to 25.85 nm, 21.83 nm, and 18.95 nm, at 80, 100, and 200 mTorr, respectively (Fig. 1b). This observed trend in the roughening behavior aligns with findings obtained in a prior work that investigated the roughness evolution of fluorinated PI surfaces under low-pressure and high-pressure oxygen plasma etching.³⁷ Given that 80 mTorr vacuum pressure parameter yielded the highest surface roughness – a 900%

increase from 2.5 nm in pristine PI to 25.85 nm in plasma-treated PI after 1 h of plasma exposure – this specific plasma treatment experimental set-up (15 cc min⁻¹ oxygen flow rate, 150 W, 80 mTorr) was selected for subsequent surface topography and wettability experiments.

3.1.2. Surface topography. The surface morphology of pristine and etched PI surfaces was examined *via* 3D holographic reconstructions as seen in Fig. 1c. The DHM results reported similar patterns in roughness evolution and provided insights into the topographical features of the PI

surfaces. Untreated PI sheets are relatively smooth (blue and yellow regions), however, after a brief-5 min exposure to oxygen plasma, few visible but non-uniform protrusions became evident (red regions). The protrusions intensify and grass-like structures start to appear after extending the etching duration to 15 min. As the treatment duration progresses, these grass-like surface morphologies expand across more extensive areas, but their non-uniformity can be attributed to varying etching rates at the different regions.

3.1.3. Surface wettability, contact angle, and chemical modifications. The wettability of plasma-treated PI surfaces was evaluated by measuring the contact angle (θ°). The contact angle of treated PI substrates showed a decreasing pattern of values with the extension of plasma duration. Fig. 1d shows the sessile drop profile on plasma-treated PI films at bias power of 85 W and 150 W, 15 cc min⁻¹ oxygen gas flow rate, and 80 mTorr pressure at different time points. While the contact angle of pristine PI Kapton sheets was around 100.86°, the contact angle was reduced drastically to 33.4° and 25.28° only after 30 sec of plasma treatment at 85 W and 150 W powers, respectively. The contact angle further decreased in substrates treated for 2 minutes to become 12.85° at 85 W and 10.35° at 150 W. After 5 min of plasma treatment at both powers, the contact angle of treated PI sheets went down to 0° as shown in Fig. 1e. Both bias power values had complete wetting effects on PI surfaces with negligible differences in contact angle measurements. Similar values were obtained for plasma-treated PI Kapton TABE and Kapton HN films when treated with oxygen plasma for 2 min at a top power of 40 W and gas flow rate of 30 cc min⁻¹.³⁸ It is worth noting the same PI substrates were assessed again five days post-plasma treatment; the contact angle greatly increased up to $\cong 50^\circ$ in all treated samples but didn't go back to their original value, as shown in Fig. 1f. Surface roughening and wettability of polymers due to plasma treatment is a consequence of many etching and chemical reaction processes including physical etching, crosslinking, and polymer chain scissions. The latter causes increments in the PI surface effective area and introduces nanoscale features, comparable to lipid bilayer dimensions, which may promote a better interface with other molecules including cells. The drastic decrease in the contact angle might be due to the plasma-induced oxygenic functional groups and/or the increments in the surface roughness of PI. For this, the chemical status of the PI surface before and after plasma treatment was inspected using FTIR transmittance spectrum, and the results are reported in Fig. 1g. The FTIR spectra of pristine and treated PI sheets exhibited several peaks around 1850, 3000, 3100, and 3200–3500 cm⁻¹ corresponding to the C=O vibration band, saturated C–H stretch, C=C carbonyl stretch, and O–H stretch, respectively. It is worth noting that no new peaks, shifts, or significant increase/decrease in original peaks were observed after etching indicating minimal chemical surface modification of plasma treated on the PI sheets. Nonetheless, it is important to declare that it is difficult to differentiate the contribution of surface functional

groups and surface roughness to the decrease in the contact angle.³⁹

3.2. Initial adhesion of neural cells cultured on plasma-roughened PI substrates: Selective attachment

SH-SY5Y and NHA were cultured on pristine PI and roughened PI surfaces (Fig. 2). For smooth PI surfaces (roughness <5 nm), the percentage of initially adherent cells was almost equivalent for both cell lines. When the surface roughness increased to approximately 15 nm, nearly all SH-SY5Y cells adhered to the rPI substrate, whereas only around 70% of NHA adhered after a 2-hour incubation period. Upon increasing the surface roughness to approximately 20 nm, SH-SY5Y cells and NHA showed a lesser percentage of initially adhering cells to rPI where almost 80% of SH-SY5Y cells adhered with major variability, and less than 40% of NHA showed initial adherence (Fig. 2a). The adapted model of cells (SH-SY5Y and NHA cells) is highly sensitive to nanoscale surface topography, and their response in terms of viability, proliferation, and even adhesion is highly dependent on the degree of roughness and feature sizes of the underlying substrate.^{31,40–42} The enhanced surface roughness and wettability by plasma etching had a positive influence on the SH-SY5Y–rPI interactions, with a preference for moderate roughness ranges ($R_a \cong 15$ nm). However, the same assimilated rPI surface features diminished initial NHA–rPI interactions. The simultaneous difference observed in neuronal and glia interaction behavior across the roughened surfaces suggests that roughness affects initial cellular interactions with the substrate in a cell-type-specific manner and can be used for selective targeting of neural cells over glia for adhesion on the implant surfaces. The latter may alleviate glial scar tissue formation over the neural interface surface by preventing astrogliosis.^{31,32}

PI often demonstrates good biocompatibility with prompt tissue integration and mild foreign body reactions.⁴³ We have previously confirmed the biocompatibility of pristine PI-based neural interfaces *in vitro* using rat PC-12 cells and neural cells extracted from embryonic cortical brain slices.^{44,45} For this current study, we evaluated the biocompatibility of plasma-etched PI sheets across various roughness ranges with both neural and glial cell lines. Visual inspection revealed that SH-SY5Y cells grown on TCP or rPI surface with $R_a \cong 15$ nm exhibited comparable proliferation rates with high cell coverage and normal morphology over 48 h as seen in Fig. 2b. After prolonged proliferation, SH-SY5Y cells establish mature focal adhesion complexes, including the non-receptor tyrosine kinase FAK and the cytoskeletal adaptor protein phospho-paxillin as demonstrated in Fig. 2c.

3.3. Single-cell force measurements of SH-SY5Y neural cells cultured on plasma-roughened PI substrates: prominent adhesion

Fluidic Force Microscopy was employed to measure the detachment forces of individual SH-SY5Y cells cultured on

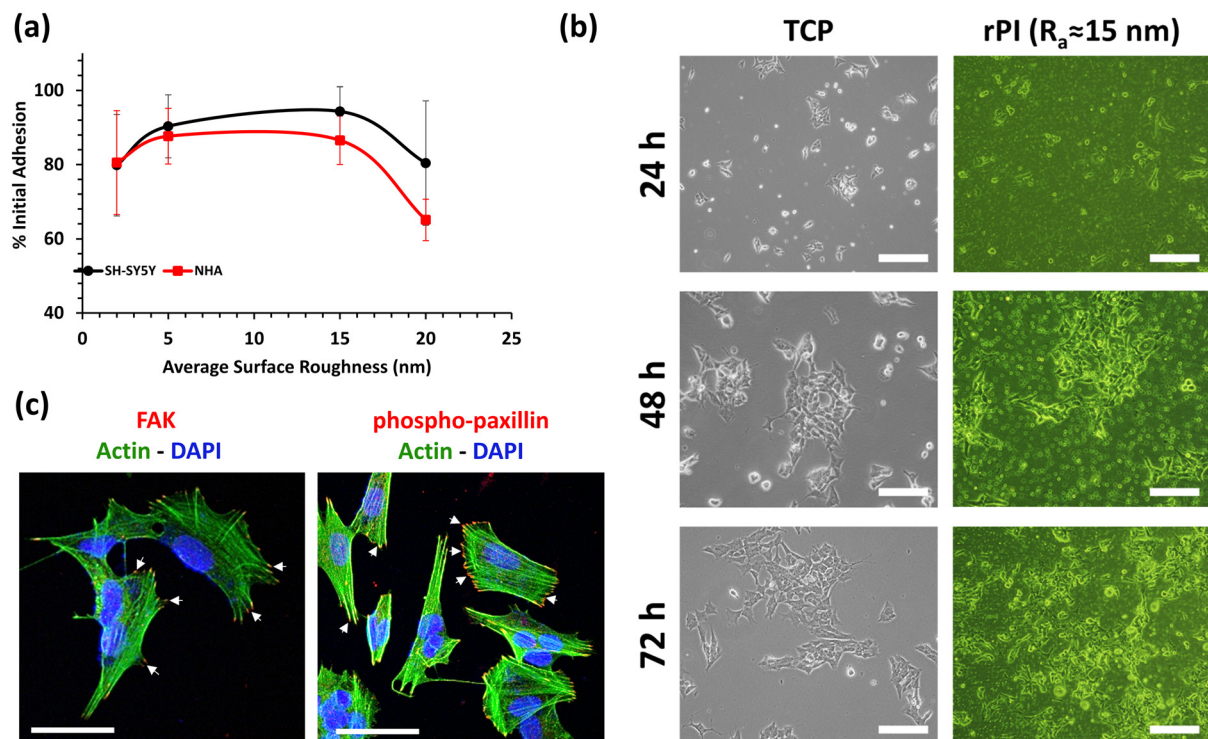


Fig. 2 Adhesion assessment of SH-SY5Y and NHA on Tissue Culture Plastic (TCP), glass coverslips (GC), and plasma-roughened polyimide (rPI) substrates. SH-SY5Y and NHA cells were cultured under 2-D conditions on TCP, CG, or rPI substrates. (a) SH-SY5Y and NHA initial adhesion were assessed 2 h post-seeding. The values depicted are the mean \pm SEM from three separate experiments. (b) Images of SH-SY5Y cells cultured on TCP ($R_a \approx 3$ nm) vs. rPI substrate ($R_a \approx 15$ nm) at different time points. Scale bar is 100 μ m. (c) Expression of actin, FAK, and phospho-paxillin in SH-SY5Y cells grown on TCP. The scale bar is 50 μ m.

TCP or rPI substrates with different surface roughness values ($R_a \approx 3$ nm, 15 nm, or 25 nm). TCP, used as the control, exhibited a surface roughness of approximately 2.8 nm, which is consistent with the nano-roughness values of polystyrene-based TCP reported previously by Zeiger *et al.*,⁴⁶ almost resembling the roughness of pristine PI substrates. On the other hand, PI substrates with nano-roughness values of 3 nm, 15 nm, and 25 nm were chosen to represent low, intermediate, and high nano-roughness levels achieved with the established dry etching treatment protocol. The PI nano-roughened sheets will be denoted as rPI₃, rPI₁₅, and rPI₂₅, respectively. TCP and rPI₃ are grouped as smooth surface controls, whereas rPI₁₅ and rPI₂₅ correspond to nano-roughened substrates. Note that smooth pristine PI sheets were excluded due to observed minimal cell attachment after 24 h of incubation. Measurements were done on single cells not in direct contact with neighboring cells to ensure that the adhesion parameters measurements solely reflect cell-substrate interactions, eliminating the interference of cell-cell contacts (intercellular junctions).

Fig. 3a provides a schematic detailing the entire cycle of cell detachment, while Fig. 3b represents the corresponding averaged characteristic force–distance curves (F – D curve) registered during the detachment of SH-SY5Y cells cultured on TCP, rPI₃, rPI₁₅, and rPI₂₅ under similar conditions and

confluency. From the F – D curves, cellular biomechanical properties can be extracted and analyzed; mainly cell-substrate adhesion strength, stiffness, and cell-substrate interaction. Key parameters derived from the F – D curves include the maximal force of adhesion (F_{adh}) which corresponds to the maximal peak force recorded during the cantilever retraction, the maximal detachment (D_{max}), which corresponds to the maximal distance traveled by the cantilever with respect to the surface at F_{adh} , and the integral of the F – D curve which represents as the adhesion work/energy (W_{adh}) required for cell detachment. The F – D curves in Fig. 3b reveal that SH-SY5Y cells demonstrate pronounced variations in their adhesion strength when grown on substrates with higher surface roughness, evident by the larger F_{adh} , W_{adh} , and D_{max} ranges as the roughness values increase. Fig. 3c and d show microscopic cellular images capturing the different stages of cell detachment by the hollow cantilever. During the SCFS experiments, a minimum of 25 adhesion curves were recorded per substrate, out of which at least 8 curves from each data set were disregarded due to weak or plain F – D curves.

The typical F – D curve characteristic parameters (F_{adh} , W_{adh} , and D_{max}) of SH-SY5Y cells cultured on the four different substrates were assessed separately and showed a lognormal distribution with an adequate fit as detailed in ESI† Table S1 and Fig. S1. Single-cell adhesion parameters

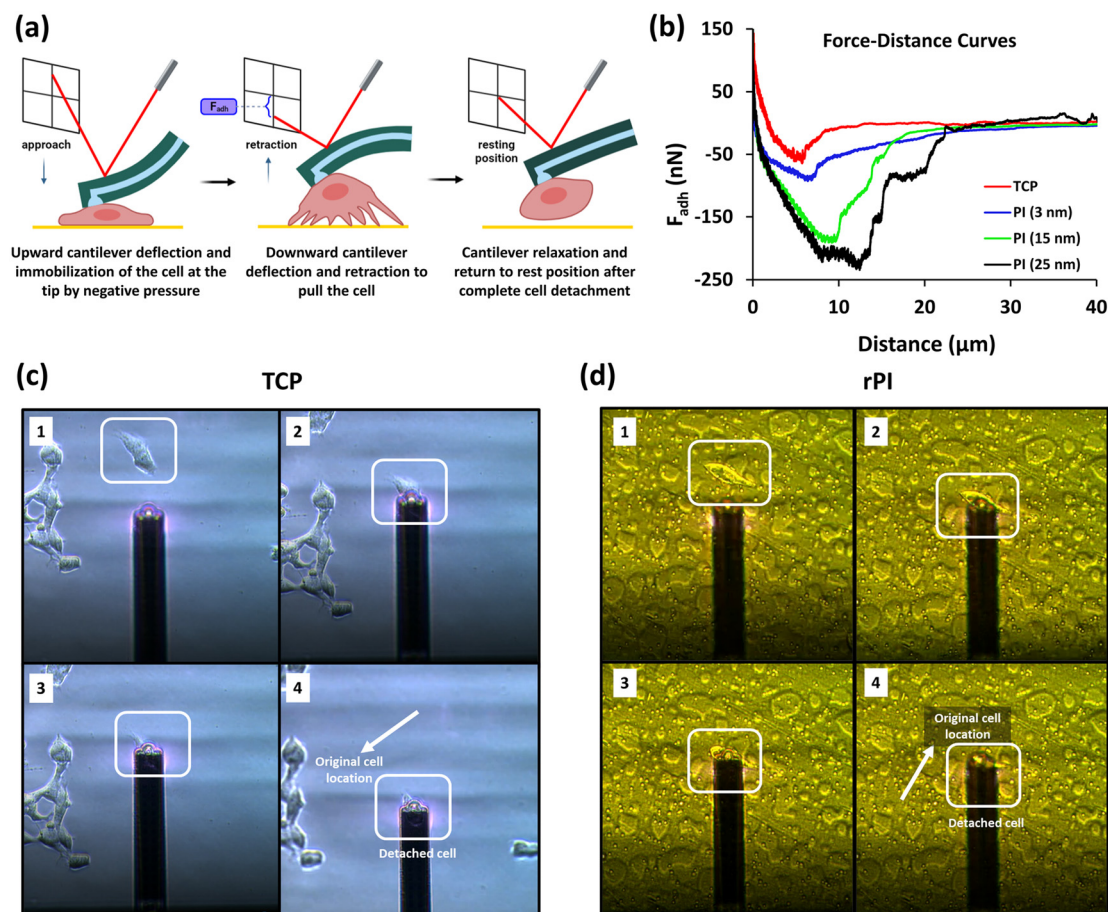


Fig. 3 Detachment evaluation of SH-SY5Y cells grown on smooth vs. rough substrates. (a) Diagram representation of the single cell force spectroscopy workflow using FluidFM method. The hollow cantilever approaches the cell until it reaches a pre-defined set point after which it immobilizes the cell by negative pressure. Once a stable contact is established, the cantilever is retracted while recording its bending and the cell is fully detached. The electrical signal of the cantilever deflection is recorded by a photodetector through the reflected laser beam (red line), and the stage position is documented by the system during the entire cycle of cell detachment to create a force–distance curve (FD-curve). (b) Representative recording of the characteristic FD-curve registered during SH-SY5Y cell detachment from the four different substrates (having smooth and rough surfaces) and its evaluation. The adhesion force is represented by the maximum peak force recorded during the cantilever deflection where the cell exerts the highest force on the cantilever. The work of adhesion energy is calculated by integrating the area under the curve from the point of contact. The maximal distance is the distance from the surface at which the cell exerts maximal force. (c and d) Bright-field images of SH-SY5Y cell detachment cycle from TCP or rPI. The four panels represent the basic steps in single-cell force spectroscopy: (1) cell localization and cantilever approach, (2) cell immobilization by negative, (3) cantilever deflection and pulling of the cell by negative pressure, (4) cantilever retraction and full cell detachment.

were evaluated and presented in box plots as shown in Fig. 4. Notably, we found strong statistical differences between SH-SY5Y cells grown on smooth surfaces (TCP and rPI_3) compared to those grown on nano-rough surfaces (rPI_{15} and rPI_{25}) as summarized in Fig. 4a–c. Specifically, SH-SY5Y cells cultured on TCP and rPI_3 had an average F_{adh} ranging between 60.7 and 107.5 nN. In contrast, SH-SY5Y cells cultured on rPI_{15} and rPI_{25} showed a significant increase in the adhesion force averaging between 150.6 and 164.6 nN, roughly a 2.5-fold increase relative to the smoother substrates. Similarly, SH-SY5Y cells cultured on smooth substrates had an average W_{adh} ranging between 0.74 and 1.6 pJ which is 2- to 3-fold lower compared to the detachment energy for cells cultured on rough substrates, averaging at 2.7 pJ. As anticipated, the D_{max} (distance traveled by the

cantilever to detach the cell) varied significantly between smooth TCP and rough PI surfaces (rPI_{15} and rPI_{25}). The average D_{max} of SH-SY5Y cells cultured on rPI_{15} and rPI_{25} was approximately 8.84 and 9.25 μm , respectively, a 0.61-fold increase compared to cells cultured on smooth TCP having an average D_{max} of 5.81 μm . In fact, cells that require a higher D_{max} to fully detach usually exert a higher F_{adh} and W_{adh} on their substrate, which is consistent with the obtained results. This is evident with D_{max} of cells grown on rPI_3 that recorded an intermediate range of D_{max} having a mean of 9.25 μm ; the recorded value aligns with the obtained intermediate F_{adh} (107.5 nN).

Our data shows that adhesion metrics (F_{adh} , W_{adh} , and D_{max}) of SH-SY5Y cells in this study are influenced by surface roughness. Upon applying a non-parametric significance test,

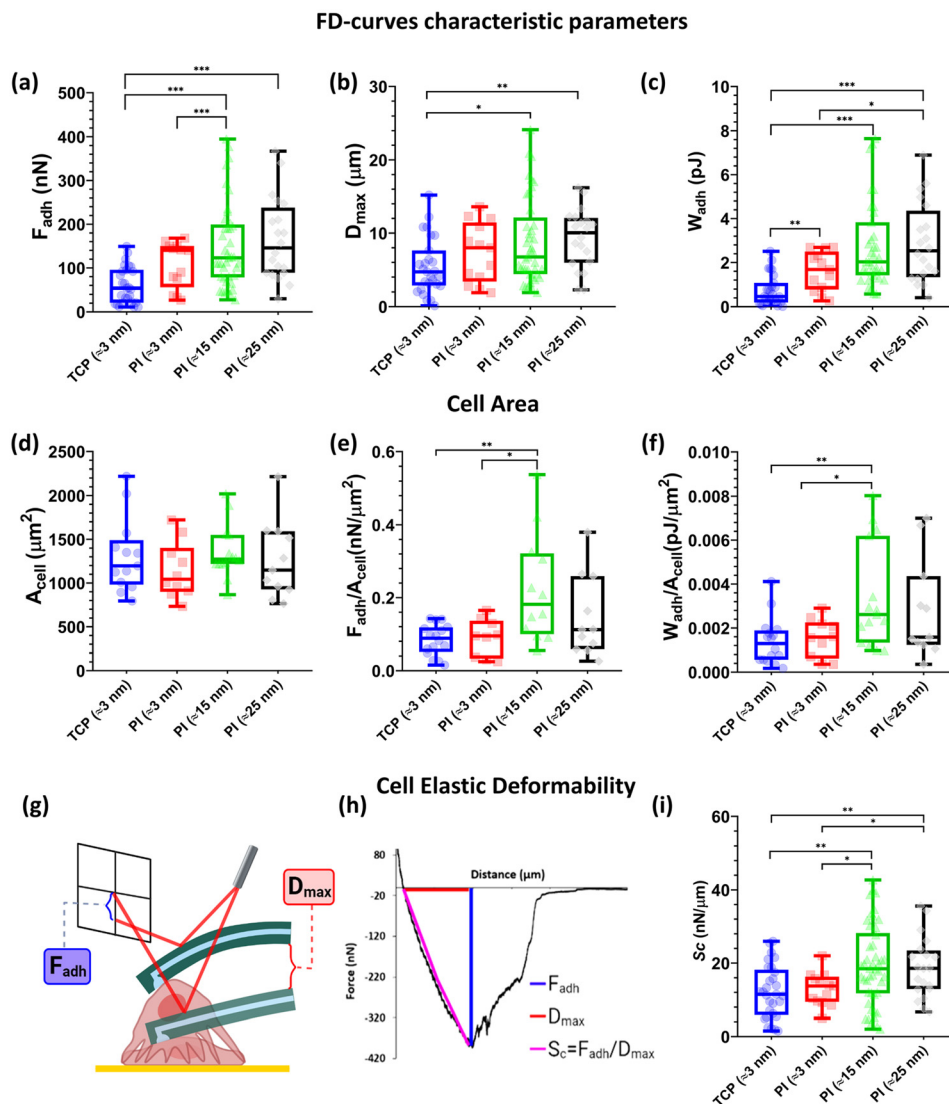


Fig. 4 Evaluation of the force–distance curve characteristic parameters and impact of cell area on the adhesion of single SH-SY5Y cells on different substrates (smooth vs. rough surfaces). (a–c) The characteristic parameters (F_{adh} , D_{max} , and W_{adh}) are represented by box plots. (d) Cell area distribution and (e and f) normalized adhesion parameters to cell area (F_{adh}/A_{cell} and W_{adh}/A_{cell}) are presented in box charts. (g) Representative schematic (not to scale) showing the elastic deformation of the cell upon pulling it from the surface using a hollow FluidFM cantilever. (h) Spring coefficient (S_c) characterizes the cell elasticity and can be interpreted from the F – D curves by calculating the fraction of F_{adh} (blue line) over D_{max} (red line) which is the linear slope (magenta line) connecting maximal force–elongation to zero level force. (i) Cell elasticity parameter distribution is a box plot. The concept of cell elasticity was adapted from ref. 26. *** denotes a p -value < 0.001, ** denotes a p -value < 0.01 and * denotes a p -value < 0.05 compared to controls for each treatment using a non-parametric two-sample Mann Whitney (unpaired, unequal variances) test.

accounting for the lognormal distribution of the cell population, most of the F – D curve parameters increased significantly when the cells were cultured on nano-roughened PI surfaces. This emphasizes that surface roughness is a key player in modulating the adhesion behavior and cellular biomechanics of SH-SY5Y cells, especially given the absence of chemical modifications as corroborated by the FTIR data (Fig. 1g). The enhancement in cell adhesion likely stems from the increased effective-to-total area of rPI, potentially allowing more contact points between the neurons and the substrate. This closer cell–surface interaction reduced the neuron–substrate gap, tightening the cell membrane–substrate seal.¹⁶

Consistent with conventional FluidFM-based SCFS data,^{23–25,47} all conditions exhibited a positive linear regression and correlation between F_{adh} – D_{max} , W_{adh} – D_{max} , and W_{adh} – F_{adh} (Fig. S2a–c†); higher forces of adhesion required greater detachment distances and larger detachment energies. Intriguingly, cells cultured on nano-rough PI surfaces compared to smooth surfaces (TCP and rPI₃), displayed a stronger correlation between F_{adh} – D_{max} and W_{adh} – D_{max} evidenced by the higher Spearman coefficient and the steeper linear regression slope confirming stronger adhesion of the cells. However, the correlation and the linear regression between F_{adh} and W_{adh} in all conditions remained consistent across all conditions, aligning with the tendency

of W_{adh} to correlate with F_{adh} (increase or decrease) at the same rate in most cases.

Furthermore, the exact cell–substrate contact area of SH-SY5Y cells, denoted as A_{cell} (in μm^2), right before cell detachment was measured. The distribution of the A_{cell} was found to be normal, and the average area was statistically similar across the investigated substrates (Fig. 4d). While SH-SY5Y cells exhibited similar spreading areas on all substrates, their overall binding strength varied, as evidenced by the normalized adhesion force and adhesion work. Interestingly, the normalized F_{adh} and W_{adh} of cells grown on rPI₁₅ showed a significant increase when compared to cells grown on smooth surfaces (Fig. 4e and f). To further investigate cell–substrate interactions, we studied the correlations between $A_{\text{cell}}-F_{\text{adh}}$, $A_{\text{cell}}-D_{\text{max}}$, and $A_{\text{cell}}-W_{\text{adh}}$ (Fig. S2d–f†). In TCP, rPI₃, and rPI₂₅ surfaces, a subtle positive correlation was revealed between cell area and force/work of adhesion, but the correlation shifted to zero in rPI₁₅ ruling out the contribution of cell size and area on the strong adherence trend observed in SH-SY5Y cells on this particular surface roughness. Remarkably, SH-SY5Y cells are highly sensitive to nanoscale features and were able to distinguish between nano-roughness values of 3 nm, 15 nm, and 25 nm, with a preference for 15 nm as an optimal topography for stronger adhesion, a peculiar nanoscale feature mimicking extracellular matrix (ECM) components and lipid bilayers of the cell membrane. Despite the lack of significant variation in cell area, many factors related to substrate topography and surface properties influence the cell–substrate interaction. The introduction of nano-features on PI with the increase in its surface wettability -due to oxygen etching- governs improved interaction between SH-SY5Y cells and the underlying rPI. Nano-roughness creates topographical signals that could induce localized changes in the cell membrane tension and cytoskeletal organization of SH-SY5Y cells affecting how these cells adhere, orient, migrate, or proliferate even if the cell spreading does not vary significantly across the substrates.⁴⁸ In addition, the increase in surface wettability of treated PI substrates makes the surface more hydrophilic and thus improves the adsorption of proteins and cell membrane into the substrate, facilitating neural cell adhesion.⁴⁹ Subsequently, the enhanced adhesion will tighten the gap between neuronal cell membranes and the underlying substrate which can be translated into a higher seal resistance (R_{seal}), a crucial parameter for designing neural interfaces with minimal leakage currents and maximal signal-to-noise ratio.⁵⁰

The F - D curve offers insights into the average elasticity of the cells being studied, inferred from their attachment strength and ability to deform. The bending of the cantilever and the longest retraction distance upon fully detaching a cell can be used to compute the spring coefficient (S_c) derived from the $F_{\text{adh}}/D_{\text{max}}$ ratio as shown in Fig. 4g and h. Of note, this parameter has been recently introduced and thoroughly explained by Nagy *et al.*²⁶ Briefly, the cell and the cantilever can be considered as two serially coupled springs, but the

cantilever coefficient is relatively large (2 N m^{-1}) and results in significantly fewer deflections compared to cell elongations. Thus, the approximated S_c from the $F_{\text{adh}}/D_{\text{max}}$ ratio essentially represents the spring coefficient of the target cell under study. The average S_c for cells grown on TCP and rPI₃ was 12.19 and 12.92 $\text{nN } \mu\text{m}^{-1}$, respectively, and are significantly smaller than that of cells grown on rPI₁₅ and rPI₂₅ substrates scoring 19.39 and 18.78 $\text{nN } \mu\text{m}^{-1}$, respectively (Fig. 4i). From a biological perspective, the resultant average S_c suggests that cells grown on nano-roughened surfaces have smaller deformation capabilities when being pulled from the surface, and thus are stiffer compared to cells grown on smoother surfaces. However, cells with shorter D_{max} are typically stiffer than cells retaining larger D_{max} ,²⁵ and accordingly, SH-SY5Y cells cultured on roughened PI surfaces appear to be more elastic because they have higher D_{max} values compared to cells grown on smooth surfaces (Fig. 4c). This apparent discrepancy in cell elasticity/stiffness can be reconciled by examining S_c values from a cell adhesion point of view. Physically, the S_c determines the “overall adhesive elasticity” of the cell influenced by the pull on the cell membrane and determined by the amount of cell–interface adhesive bonds (focal adhesion complexes and corresponding receptor–ligand bonds). These adhesion bonds are tightened when the gap between the cell and the underlying rPI substrates diminishes leading to an intimate cell–substrate attachment. As such, while SH-SY5Y cells cultured on nano-roughened PI surfaces appear to be quantitatively stiffer (based on the elevated S_c values), they are elastic and have considerable elongation capabilities indicated by longer cantilever retractions (larger D_{max}) to fully detach the strongly adherent cells, confirming a strong attachment.

Conclusions and outlooks

Intimate cell adhesion to neural implant surfaces is a major factor in determining both the longevity of the implanted device and its proper integration with the surrounding tissue. In this work, we provide key insights into how surface topography influences neural cell adhesion. Our comprehensive analysis, encompassing initial adhesion and FluidFM-based SCFS data showed a significant improvement of SH-SY5Y cell adhesion to roughened surfaces, almost two orders of magnitudes in most parameters, without affecting cell proliferation, spreading, or overall cell–interface contact area. The variation in the adhesion behavior and neural biomechanical cues of SH-SY5Y cells cultured on either smooth or rough substrates likely stems from alterations in roughness (*i.e.*, effective surface area) and/or wettability of PI films introduced by plasma treatment.⁶

It is generally accepted that roughened surfaces can optimize the integration, durability, and performance of neural implant materials, fostering robust adhesion of neural cells.^{31,32,51–53} The improved intimate adhesion of neural cells to the underlying substrates could, subsequently, govern

a tighter cell–substrate interface, a key factor in achieving high seal resistance. The latter will potentially minimize leakage current and enhance signal fidelity, especially in the case of flat electrodes used in neural recording and stimulation devices.⁵⁴ Additionally, our findings have implications in the case of neural implants with penetrating electrodes. The improvement of neural cell adhesion on roughened substrates could facilitate the insertion of needle electrodes and maintain stable intracellular recordings, as adequate adhesion is essential to prevent impedance and maintain signal stability.¹⁶

The results in this framework suggest that the nanotopography of PI surfaces plays a critical role in determining cellular responses related to adhesion. Our findings recommend a quantitative framework for tailoring the surface topography of polyimide-based implants for improved neural adhesion. The proximity of neurons to the polyimide-based devices promises improved signal transduction fidelity, characterized by a high signal-to-noise ratio and minimized power requirements for recording and stimulating electrogenic cells.

Author contributions

The manuscript includes contributions from all authors. The authors have all approved the final version of the manuscript upon submission. M. K. conceived the idea, designed the study and experiments, supervised experimental protocols and analysis for cell culture, FluidFM, and fabrication, and supervised the content and writing and funded the work. Z. H. wrote the manuscript, performed biomechanical cell adhesion experiments with the FluidFM OMNIUM system and statistically analyzed the data. R. L. performed polyimide substrates plasma treatment and assessed their biocompatibility to neural cells and astrocytes, and performed the biomechanical cell adhesion experiments. W. A. K. supervised immunofluorescence assisted in cell culture and reviewed the manuscript. Z. H. and A. Z. extracted the F - D curves and corresponding parameters in AtomicJ and MATLAB, after which they cleaned the data and plotted it in GraphPad Prism 8.0.1 and OriginPro 9.5.

Conflicts of interest

None of the authors state any form of conflict of interest.

Acknowledgements

The authors acknowledge funding from Maroun Semaan research initiative and the University Research Board (URB).

References

- 1 M. Zhang, Z. Tang, X. Liu and J. van der Spiegel, *Nat. Electron.*, 2020, **3**, 191–200.
- 2 N. G. Hatsopoulos and J. P. Donoghue, *Annu. Rev. Neurosci.*, 2009, **32**, 249–266.
- 3 W. C. Stacey and B. Litt, *Nat. Clin. Pract. Neurol.*, 2008, **4**, 190–201.
- 4 B. Rubehn and T. Stieglitz, *Biomaterials*, 2010, **31**, 3449–3458.
- 5 J. Viventi, D. H. Kim, L. Vigeland, E. S. Frechette, J. A. Blanco, Y. S. Kim, A. E. Avrin, V. R. Tiruvadi, S. W. Hwang, A. C. Vanleer, D. F. Wulsin, K. Davis, C. E. Gelber, L. Palmer, J. van der Spiegel, J. Wu, J. Xiao, Y. Huang, D. Contreras, J. A. Rogers and B. Litt, *Nat. Neurosci.*, 2011, **14**, 1599–1605.
- 6 C. P. Constantin, M. Aflori, R. F. Damian and R. D. Rusu, *Materials*, 2019, **12**.
- 7 S. van Vlierberghe, M. Sirova, P. Rossmann, H. Thielecke, V. Boterberg, B. Rihova, E. Schacht and P. Dubrue, *Biomacromolecules*, 2010, **11**, 2731–2739.
- 8 S. Myllymaa, K. Myllymaa, H. Korhonen, M. J. Lammi, V. Tiitu and R. Lappalainen, *Colloids Surf., B*, 2010, **76**, 505–511.
- 9 L. Astoreca, P. Cools, D. Schaubroeck, M. Asadian, S. Aliakbarshirazi, H. Declercq, M. O. de Beeck, H. de Smet and N. de Geyter, *Polymer*, 2020, **205**, 122831.
- 10 M. R. Vasquez, E. I. Prieto, M. Wada, D. Bldg and V. C. S. cor Garcia, *Radio-Frequency Plasma-Induced Biocompatibility of Polyimide Substrates*, 2018, vol. 8.
- 11 S. Nagaoka, K. Ashiba and H. Kawakami, *Mater. Sci. Eng., C*, 2002, **20**, 181–185.
- 12 N. Jackson, L. Keeney and A. Mathewson, *Smart Mater. Struct.*, 2013, **22**(11), 115033.
- 13 H. Kawakami, K. Hiraka, S. Nagaoka, Y. Suzuki and M. Iwaki, *J. Artif. Organs*, 2004, **7**, 83–90.
- 14 F. Kristian, P. A. Janmey and G. Jochen, *Annu. Rev. Biomed. Eng.*, 2013, **15**, 227–251.
- 15 R. J. Leiphart, D. Chen, A. P. Peredo, A. E. Loneker and P. A. Janmey, *Langmuir*, 2019, **35**, 7509–7519.
- 16 M. L. Khraiche and R. El Hassan, *J. Sci.: Adv. Mater. Devices*, 2020, **5**, 279–294.
- 17 S. Di Cio and J. E. Gautrot, *Acta Biomater.*, 2016, **30**, 26–48.
- 18 M. Benoit, D. Gabriel, G. Gerisch and H. E. Gaub, *Discrete interactions in cell adhesion measured by single-molecule force spectroscopy*, 2000, vol. 2.
- 19 J. Friedrichs, K. R. Legate, R. Schubert, M. Bharadwaj, C. Werner, D. J. Müller and M. Benoit, *Methods*, 2013, **60**, 169–178.
- 20 S. Xia and P. Kanchanawong, *Semin. Cell Dev. Biol.*, 2017, **71**, 53–67.
- 21 M. Li, L. Liu and T. Zambelli, *Nano Res.*, 2022, **15**, 773–786.
- 22 P. Saha, T. Duanis-Assaf and M. Reches, *Adv. Mater. Interfaces*, 2020, **7**.
- 23 A. G. Nagy, A. Bonyar, I. Szekacs and R. Horvath, in *2020 IEEE 26th International Symposium for Design and Technology in Electronic Packaging, SIITME 2020 - Conference Proceedings*, Institute of Electrical and Electronics Engineers Inc., 2020, pp. 21–25.
- 24 P. Dörig, P. Stiefel and P. Behr, *Appl. Phys. Lett.*, 2010, **97**, 23701.
- 25 Á. G. Nagy, I. Székács, A. Bonyár and R. Horvath, *Eur. J. Cell Biol.*, 2022, **101**, 151273.
- 26 Á. G. Nagy, N. Kanyó, A. Vörös, I. Székács, A. Bonyár and R. Horvath, *Sci. Rep.*, 2022, **12**(1), 7747.

- 27 M. Sztilkovics, T. Gerecsei, B. Peter, A. Saftics, S. Kurunczi, I. Szekacs, B. Szabo and R. Horvath, *Sci. Rep.*, 2020, **10**(1), 61.
- 28 M. Luo, W. Yang, T. N. Cartwright, J. M. G. Higgins and J. Chen, *Langmuir*, 2022, **38**, 620–628.
- 29 A. Sancho, I. Vandersmissen, S. Craps, A. Lutun and J. Groll, *Sci. Rep.*, 2017, **7**(1), 46152.
- 30 N. Cohen, S. Sarkar, E. Hondroulis, P. Sabhachandani and T. Konry, *Talanta*, 2017, **174**, 409–413.
- 31 V. Brunetti, G. Maiorano, L. Rizzello, B. Sorce, S. Sabella, R. Cingolani and P. P. Pompa, *Proc. Natl. Acad. Sci. U. S. A.*, 2010, **107**, 6264–6269.
- 32 C. A. R. Chapman, H. Chen, M. Stamou, J. Biener, M. M. Biener, P. J. Lein and E. Seker, *ACS Appl. Mater. Interfaces*, 2015, **7**, 7093–7100.
- 33 Á. G. Nagy, J. Kámán, R. Horváth and A. Bonyár, DOI: [10.1038/s41598-019-46691-x](https://doi.org/10.1038/s41598-019-46691-x).
- 34 Y. Tian, W. Liu and L. Hang, *Phys. Procedia*, 2011, **18**, 107–111.
- 35 M. Cen-Puc, A. Schander, M. G. V. Gleason and W. Lang, DOI: [10.3390/polym13121955](https://doi.org/10.3390/polym13121955).
- 36 R. Flitsch and D. Shih, *J. Vac. Sci. Technol.*, A, 1990, **8**, 2376–2381.
- 37 N. Agarwal, S. Ponoht, J. Plawsky and P. D. Persans, *Appl. Phys. Lett.*, 2001, **78**, 2294–2296.
- 38 H. Kizil, M. O. Pehlivaner and L. Trabzon, in *Advanced Materials Research*, Trans Tech Publications Ltd, 2014, vol. 970, pp. 132–135.
- 39 F. Lin, W. Li, Y. Tang, H. Shao, C. Su, J. Jiang and N. Chen, *Polymers*, 2018, **10**(7), 695.
- 40 N. R. Blumenthal, O. Hermanson, B. Heimrich and V. P. Shastri, *Proc. Natl. Acad. Sci. U. S. A.*, 2014, **111**, 16124–16129.
- 41 I. Tonazzini, A. Cecchini, Y. Elgersma and M. Cecchini, *Adv. Healthcare Mater.*, 2014, **3**, 581–587.
- 42 M. Lecchi, P. A. Wieringa, R. Lutge, A. Bastiaens and R. Sabahi-Kaviani, DOI: [10.3389/fnins.2020.00666](https://doi.org/10.3389/fnins.2020.00666).
- 43 N. Lago, K. Yoshida, K. P. Koch and X. Navarro, *IEEE Trans. Biomed. Eng.*, 2007, **54**, 281–290.
- 44 R. M. Almasri, W. Alchamaa, A. R. Tehrani-Bagha and M. L. Khraiche, *ACS Appl. Bio Mater.*, 2020, **3**, 7040–7051.
- 45 M. L. Khraiche, W. B. Phillips, N. Jackson and J. Muthuswamy, *Microsyst. Technol.*, 2017, **23**, 3671–3683.
- 46 A. S. Zeiger, B. Hinton and K. J. van Vliet, *Acta Biomater.*, 2013, **9**, 7354–7361.
- 47 S. Sankaran, L. Jaatinen, J. Brinkmann, T. Zambelli, J. Vörös and P. Jonkheijm, *ACS Nano*, 2017, **11**, 3867–3874.
- 48 E. Martínez, E. Engel, J. A. Planell and J. Samitier, *Ann. Anat.*, 2009, **191**, 126–135.
- 49 S. Cai, C. Wu, W. Yang, W. Liang, H. Yu and L. Liu, *Nanotechnol. Rev.*, 2020, **9**, 971–989.
- 50 A. Blau, *Curr. Opin. Colloid Interface Sci.*, 2013, **18**, 481–492.
- 51 R. Ding, N. C. Miller, K. M. Woepfel, X. T. Cui and T. D. B. Jacobs, *Langmuir*, 2022, **38**, 7512–7521.
- 52 K. Baranes, M. Shevach, O. Shefi and T. Dvir, DOI: [10.1021/acs.nanolett.5b04033](https://doi.org/10.1021/acs.nanolett.5b04033).
- 53 M. L. Khraiche, J. Rogul and J. Muthuswamy, *Front. Neurosci.*, 2019, **13**, 518.
- 54 M. Khraiche and J. Muthuswamy, *Lab Chip*, 2012, **12**, 2930–2941.